RSC Advances

PAPER

View Article Online
View Journal | View Issue

Cite this: *RSC Adv.*, 2025, **15**, 46692

Exploring vivid red light emanating europium complexes incorporating a β-ketoester antenna for advanced displays: a detailed photophysical, Judd–Ofelt and computational investigation

Nishita Dua and Priti Boora Doon *

Five new organo-europium samples consisting of β-ketoester (diethyl oxalpropionate) together with secondary sensitizers (neocuproine, bathophenanthroline, 1,10-phenanthroline and 4,4′-dimethyl-2,2′-bipyridyl) were successfully synthesized as well as characterized. The structural compositions of the samples were elucidated using EDAX and elemental analysis. The PXRD profile disclosed the crystalline nature of the samples, and the surface morphology possessing rod-shaped agglomerates was further confirmed by the FESEM micrograph. The complexation of Eu(III) with DO occurs *via* the O atom of the C=O moiety, as indicated by FT-IR spectroscopy and NMR spectroscopy investigations. The theoretical evaluation of the optical band gap using DFT aligns closely with the values derived experimentally from Tauc plots. The band gap range of 3.36–3.79 eV indicates its applicability in semiconductors. The emission spectra procured by exciting the samples at 360 nm portrayed peaks at 655, 616, 596 and 584 nm associated with $^5D_0 \rightarrow {}^7F_J$ (J = 3, 2, 1, 0, respectively) transitions. The pronounced red photoluminescence is mainly governed by the prominent $^5D_0 \rightarrow {}^7F_2$ transition of the Eu(III) ions. The photophysical parameters of the samples were further analysed to evaluate the photoluminescence decay time, Judd–Ofelt intensity parameter, intrinsic quantum efficiency, and radiative and nonradiative decay rates. Colorimetric investigations authenticate these samples as warm red light emitters, validating their promising utility as red components in light emitting sources. A study of the energy transmission pathway revealed a correlation between the triplet state of the sensitizers and the resonating levels of the metal center. These results highlight the incredible potential of these luminous europium samples for photonic and display devices.

Received 10th September 2025
Accepted 12th November 2025

DOI: 10.1039/d5ra06840a

rsc.li/rsc-advances

1 Introduction

Currently, the world is facing an unprecedented rise in energy expenditures. Therefore, to preserve energy, scientists and researchers are investing significant efforts in developing SSL (solid-state lighting) devices.[1] These devices can be fabricated by coating them with luminescent lanthanide complexes. In 1942, the first luminescent lanthanide complex was investigated by Weissman.[2] Since then, a plethora of studies have been reported on luminescent lanthanide complexes due to their fascinating applications, such as light generators, luminescent thermometers, electroluminescent devices, liquid crystalline materials, agriculture, audio applications, chemical sensing and single-molecule magnets.[3–8] Lanthanide complexes remain in the limelight owing to their intriguing photoluminescence attributes such as a large shift in energy between emitted and absorbed radiation, longer photoluminescence lifetime, monochromatic emission and higher quantum efficiency.[9–11]

Lanthanide ions [Ln(III)] have a characteristic fingerprint spectrum because the 4f energy levels are shielded by the 5s and 5p subshells; hence, the chemical environment around the lanthanide ions has very little impact on the energetic positions of the transitions.[12] However, lanthanide ions have low absorption coefficients because it is forbidden for electrons to redistribute within the same subshell as per the Laporte rule.[13,14] To circumvent this bottleneck, the Ln(III) ion is coordinated with an organic chromophore with a high absorption coefficient.[15] This organic chromophore serves as an antenna to harvest the energy absorbed by the Ln(III) ion.[16,17] Thus, for the successful transfer of energy, the levels of the employed organic chromophore must be compatible with the energy levels of the lanthanide ion.[18] Among the range of organic ligands, β-ketoester remains at the forefront because it effectively transfers energy to the central metal ion.[19,20] The coordination number exhibited by Ln(III) ions is generally 8, with 6 sites occupied by the DO ligand and the rest are employed by either solvent or

Department of Chemistry, Maharshi Dayanand University, Rohtak-124001, India. E-mail: pritiboora@gmail.com; Tel: +91-9416175000

water molecules.[21,22] The existence of O–H and N–H oscillators in water or solvent molecules intensifies radiationless deactivation and reduces the photoluminescence intensity of the complexes.[23,24] Therefore, to get rid of this deleterious aspect, these lanthanide complexes are complexed with O- or N-donor secondary ligands.[25–27] These secondary ligands expel the solvent or water molecules from the inner coordination sphere and work synergistically with DO to enhance the photoluminescence intensity.[28–30] Hence, considering the information mentioned above, synthesis of five Eu(III) complexes was accomplished by preferring diethyl oxalpropionate (DO) as the main sensitizer and bathophenanthroline (batho), neocuproine (neo), 1,10-phenanthroline (phen) and 4,4′-dimethyl-2,2′-bipyridyl (dmbipy) as secondary sensitizers. The europium complexes synthesized are represented as $[Eu(DO)_3(H_2O)_2]$ (E1), $[Eu(DO)_3neo]$ (E2), $[Eu(DO)_3dmbipy]$ (E3), $[Eu(DO)_3batho]$ (E4) and $[Eu(DO)_3phen]$ (E5).

The metal–ligand skeleton of the synthesized Eu(III) samples was demonstrated *via* Proton FT-IR (Fourier transform infrared spectroscopy), NMR (proton nuclear magnetic resonance), EDAX (energy dispersive X-ray analysis) and CHN analysis. The crystalline attributes and surface morphology of the europium samples were determined using PXRD and FESEM analyses. Thermogravimetric analysis was performed to investigate the thermal behaviour of the synthesized samples. The photoluminescence attributes of the samples were explored by diffuse reflectance (DR), UV-visible absorption and photoluminescence (PL) studies. The band gap of the samples was assessed *via* Tauc plots, which was further supported by DFT studies. The Judd–Ofelt parameters and internal quantum efficiency of the luminous samples were determined using photoluminescence emission data. The pathway of energy transmission in the europium samples was also examined.

2 Experimental section

2.1 Materials

The compounds $[Eu(NO_3)_3\cdot 6H_2O]$, diethyl oxalpropionate and $[Gd(NO_3)_3\cdot 6H_2O]$ were obtained from Sigma-Aldrich and were utilized as received. The solvents availed were of analytical grade and were used as such unless otherwise specified.

2.2 Synthesis of binary hydrated samples

A solution of DO (3 mmol) in ethanol was added to a solution of $[Eu(NO_3)_3\cdot 6H_2O]$ (1 mmol) in H_2O while stirring. The pH of this reaction mixture was maintained within 6.5–7 by adding a solution of NaOH. Then, by heating a magnetic stirrer, this reaction mixture was constantly stirred and heated for 3 h at 110 °C. Finally, the solid residue of E1 $[Eu(DO)_3(H_2O)_2]$ was collected after the complete evaporation of solvent.[31] Furthermore, the synthesis of the $[Gd(DO)_3\cdot 2H_2O]$ (G1) complex was carried out using a similar procedure.

2.3 Synthesis of ternary samples

The E2–E5 samples were synthesized using the same procedure as the E1 complex, but for the synthesis of ternary complexes, a 3 mmol solution of DO and 1 mmol solution of secondary ligands in C_2H_5OH were added to a 1 mmol solution of $[Eu(NO_3)_3\cdot 6H_2O]$ in distilled water. Lanthanide ions usually prefer a coordination number of 8. Therefore, a 3 : 1 : 1 stoichiometry was employed, as the bidentate chelating sensitizer DO occupies 6 coordination sites, while the secondary sensitizers occupy the other 2 sites. This ratio thus ensures a rigid coordination environment and maintains the charge neutrality in the samples. The secondary ligands suppress nonradiative deactivation by displacing the coordinated water molecules. The secondary ligands availed for the E2–E5 samples sequentially were neo, dmbipy, batho and phen. The pathway of synthesis and the chemical framework of DO and E1–E5 are depicted in Scheme 1.

$[Eu(DO)_3\cdot 2H_2O]$ (E1): FT-IR (cm^{-1}, KBr pellet): 470 (w), 1198 (m), 1657 (w), 1729 (m); proton NMR (500 MHz, DMSO): δ 3.89 (q, 6H, $-CH_2$), 3.44 (q, 6H, $-CH_2$), 3.34 (d, 4H, H_2O), 0.73 (t, 9H, $-CH_3$), 2.47 (s, 9H, $-CH_3$), 1.02 (t, 9H, $-CH_3$) ppm.

$[Eu(DO)_3(neo)]$ (E2): FT-IR (cm^{-1}, KBr pellet): 481 (w), 557 (w), 1203 (m), 1533 (m), 1669 (w), 1741 (m); proton NMR (500 MHz, DMSO): δ 8.58 (d, 2H, Ar–H), 3.40 (q, 6H, $-CH_2$), 1.01 (t, 9H, $-CH_3$), 0.69 (t, 9H, $-CH_3$), 2.42 (s, 9H, $-CH_3$), 3.93 (q, 6H, $-CH_2$), 7.94 (s, 2H, Ar–H), 2.50 (s, 6H, $-CH_3$), 7.27 (d, 2H, Ar–H) ppm.

$[Eu(DO)_3(dmbipy)]$ (E3): FT-IR (cm^{-1}, KBr pellet): 473 (w), 582 (w), 1194 (m), 1523 (m), 1662 (w), 1735 (m); proton NMR (500 MHz, DMSO): δ 8.71 (d, 2H, Ar–H), 2.48 (s, 9H, $-CH_3$), 1.04 (t, 9H, $-CH_3$), 3.95 (q, 6H, $-CH_2$), 8.45 (d, 2H, Ar–H), 0.71 (t, 9H, $-CH_3$), 7.29 (d, 2H, Ar–H), 2.43 (s, 6H, $-CH_3$), 3.47 (q, 6H, $-CH_2$), ppm.

$[Eu(DO)_3(batho)]$ (E4): FT-IR (cm^{-1}, KBr pellet): 479 (w), 580 (w), 1197 (m), 1527 (m), 1676 (w), 1744 (m); proton NMR (500 MHz, DMSO): δ 1.14 (t, 9H, $-CH_3$), 7.90 (m, 10H, Ar–H), 4.02 (q, 6H, $-CH_2$), 2.56 (s, 9H, $-CH_3$), 8.72 (m, 4H, Ar–H), 0.83 (t, 9H, $-CH_3$), 9.21 (d, 2H, Ar–H), 7.76 (s, 2H, Ar–H), 3.60 (q, 6H, $-CH_2$) ppm.

$[Eu(DO)_3(phen)]$ (E5): FT-IR (cm^{-1}, KBr pellet): 482 (w), 585 (w), 1200 (m), 1519 (m), 1667 (w), 1738 (m); proton NMR (500 MHz, DMSO): δ 2.54 (s, 9H, $-CH_3$), 3.97 (q, 6H, $-CH_2$), 0.77 (t, 9H, $-CH_3$), 8.68 (m, 4H, Ar–H), 9.16 (d, 2H, Ar–H), 7.96 (s, 2H, Ar–H), 3.53 (q, 6H, $-CH_2$), 1.08 (t, 9H, $-CH_3$) ppm.

3 Results and discussion

3.1 Composition of the samples

Ametek EDAX was utilized to analyse the elemental mapping and spectra of the europium complexes. The peaks obtained in the EDAX spectra indicate that the coordination scaffold of E1–E5 complexes consists of N, C, Eu and O. The elemental mapping and spectra of the E5 complex are depicted in Fig. 1(a) and (b), respectively. The amount (%) of nitrogen, hydrogen and carbon was obtained by employing a PerkinElmer 2400 CHN elemental analyser. Furthermore, complexometric titrations were carried out to obtain the percentage of Eu(III) ions in the E1–E5 complexes. The results obtained were equipollent to the proposed formulae. Table 1 illustrates the amount (%) of europium, nitrogen, hydrogen and carbon.

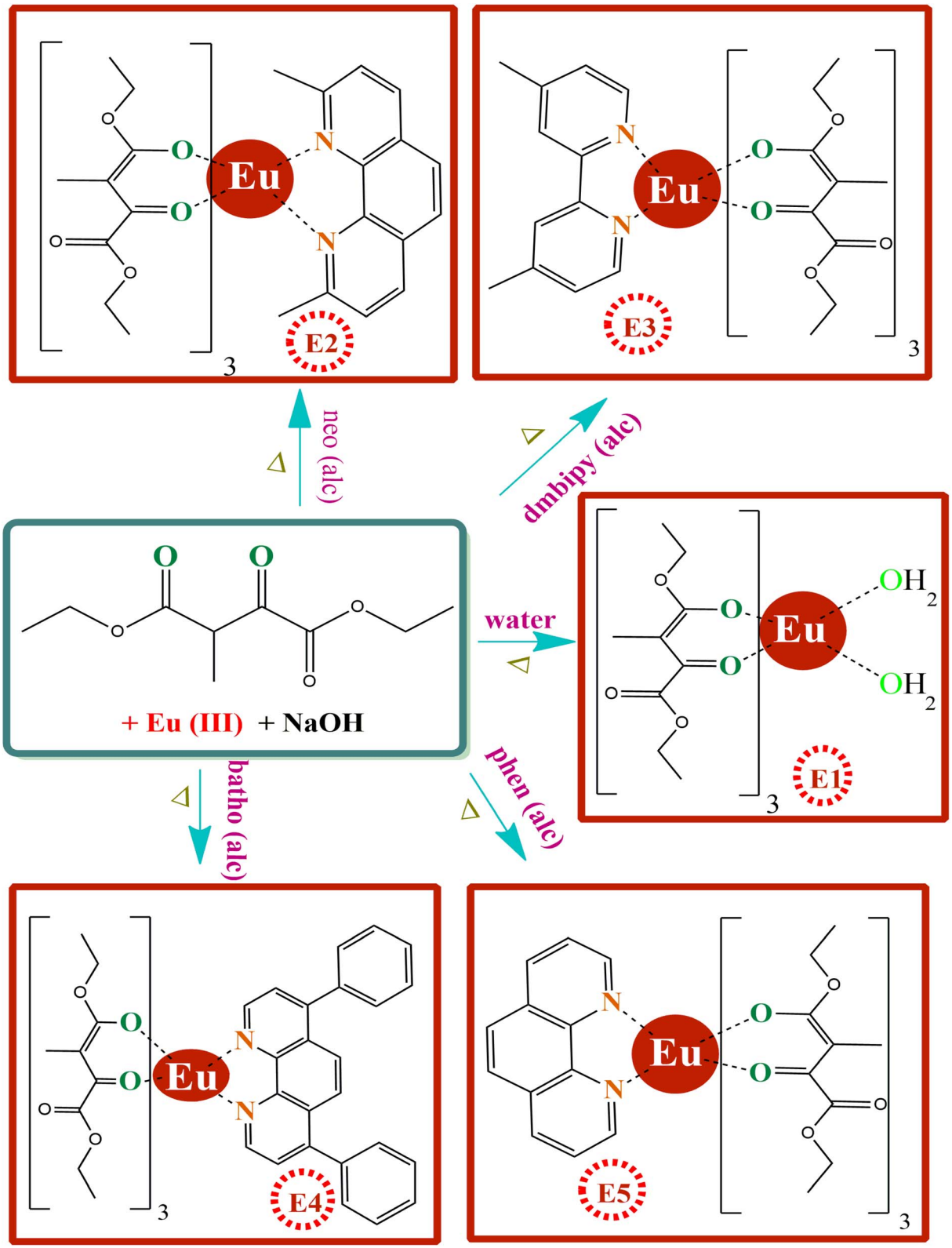

Scheme 1 The synthetic pathway and chemical structure of DO and the E1–E5 samples.

3.2 XRD analysis

X-ray diffraction (XRD) analysis was employed to examine the crystalline nature of the europium-based samples. The analysis was conducted over a 2θ Bragg's angle ranging from 10° to 80°. Fig. 2(a) illustrates the XRD spectrum of the E5 sample. The diffractogram exhibits distinct and sharp peaks, indicating the

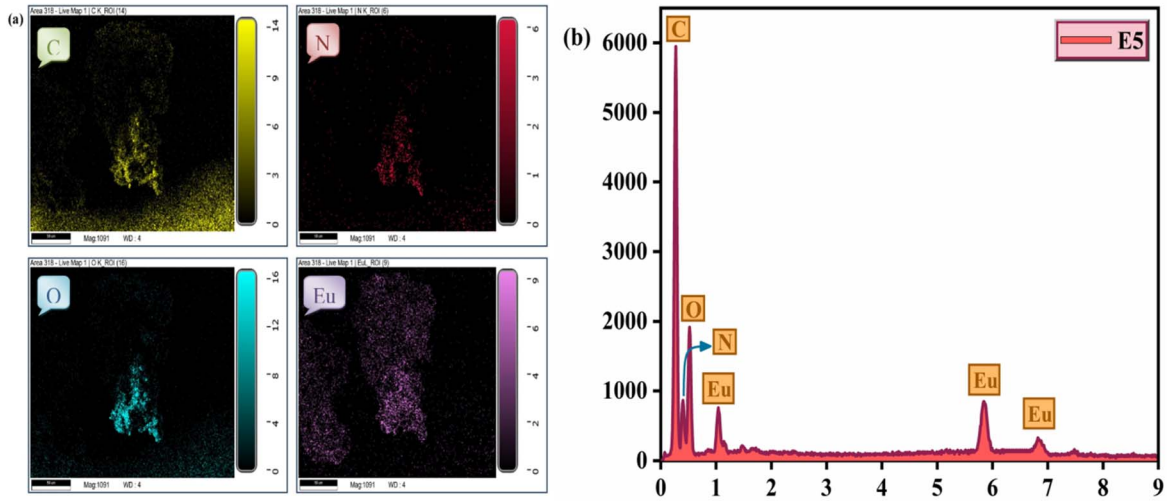

Fig. 1 (a) EDAX mapping displaying the elements Eu, N, C and O of E5 [Eu(DO)$_3$phen]. (b): EDAX spectrum of E5 [Eu(DO)$_3$phen].

pronounced crystallinity of the samples. The pronounced peaks in the XRD pattern of E5 are observed at 11.68°, 12.63°, 13.45°, 14.26°, 19.49°, 29.50°, 32.14°, 36.03°, 39.81°, 43.44° and 48.86°. Further, the analysis of the XRD data determined a crystallinity index of 64.67% computed by dividing the integrated area of prominent peaks by the integrated area of the entire diffractogram. The crystallinity index reveals its potential utility in photonic devices.

To determine the average crystallite size of the E5 sample, the widely recognized Scherrer's equation was used, as stated below:[32]

$$D = \frac{k\lambda}{\beta \cos \theta}, \quad (1)$$

where D represents the average size of crystallite, β is FWHM (full width at half maxima) of the most prominent diffraction peak, k is Scherrer's constant, θ represents the position of the diffraction peak and λ represents the wavelength of the incident X-ray radiation. The analysis of the PXRD data revealed the crystallite size of the E5 sample to be 50.28 nm. This size is comparable with the data reported by Chhillar *et al.*[33] and Gaur *et al.*.[34]

Furthermore, the dislocation density (ρ) was determined to evaluate the lattice imperfections using the following relation:[35]

$$\rho = \frac{1}{D^2}. \quad (2)$$

The dislocation density (ρ) was determined to be 3.96×10^{14} m^{-2}, revealing a moderate degree of defects within the crystal lattice. The value of ρ indicates the degree of lattice defects that lead to the broadening of peaks, and it offers valuable information on the quality of the crystal, which plays a crucial role in determining the physicochemical as well as mechanical behaviour of the sample.

3.3 FESEM analysis

The morphological aspects of the europium samples were thoroughly investigated utilizing FESEM (field emission scanning electron microscopy). The FESEM micrograph reveals a homogenous surface morphology characterized by rod-like aggregates. These morphological features suggest the crystalline nature of the samples, which is further corroborated by the PXRD results. The ordered structural aspects of these samples indicate their applicability in advanced optoelectronic devices.[36] Fig. 2(b) illustrates the FESEM image of [Eu(DO)$_3$phen].

3.4 FT-IR spectral studies

The Nicolet iS50 FT-IR spectrophotometer was employed to record the FT-IR spectral data of DO and europium samples from KBr discs within the operating span of 4000–400 cm^{-1}. In the FT-IR window of free DO, the stretch frequencies for the carbonyl group of keto and ester functionalities are detected at 1654 cm^{-1}

Table 1 Elemental composition of the DO and europium samples in terms of weight %

Complex	C (%) found (cal)	H (%) found (cal)	N (%) found (cal)	Eu (%) found (cal)
DO	53.47 (53.46)	6.99 (6.98)	—	—
E1	41.33 (41.28)	4.72 (4.75)	—	19.39 (19.34)
E2	51.35 (51.42)	4.81 (4.74)	2.99 (2.92)	15.78 (15.87)
E3	50.21 (50.17)	4.93 (4.86)	3.12 (3.00)	16.33 (16.27)
E4	56.71 (56.62)	4.50 (4.56)	2.47 (2.59)	14.11 (14.04)
E5	50.29 (50.38)	4.35 (4.44)	3.09 (3.01)	16.28 (16.34)

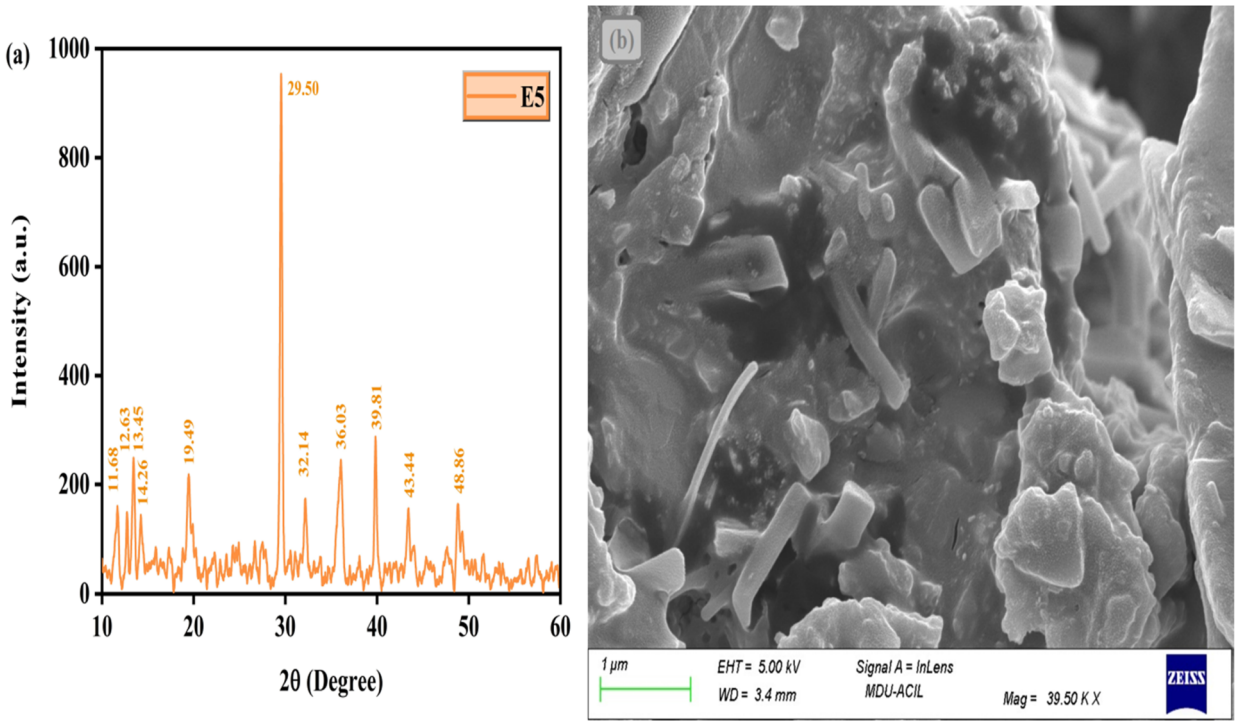

Fig. 2 (a): Powder X-ray diffraction pattern of E5 [Eu(DO)$_3$phen]. (b) FESEM micrograph of E5 [Eu(DO)$_3$phen].

and 1717 cm^{-1}, respectively. Moreover, the stretch frequencies of C–O and C–H are detected at 1217 cm^{-1} and 2968 cm^{-1}, respectively. The FT-IR spectra of europium-based samples exhibit distinct bands between 1744 and 1729 cm^{-1} attributed to the stretch frequencies of the C=O group of keto and ester moieties, respectively. The noticeable shifting of the vibrational bands in the E1–E5 samples suggests compelling evidence for the participation of C=O in the complexation of DO with Eu^{3+} ions. The coordination of primary sensitizer and Eu(III) ions through carbonyl functionalities is further confirmed by the appearance of new bands within the 482–470 cm^{-1} range, which is attributed to Eu–O stretch frequencies.[37] Furthermore, the existence of prominent bands within 585–577 cm^{-1} and 1533–1519 cm^{-1} ranges associated with the stretch modes of Eu–N and C=N linkage, respectively, revealed the coordination of Eu(III) ions with secondary sensitizers in E2–E5 samples.[38] In the spectrum of the E1 sample, the detection of a band at 3437 cm^{-1} indicates the presence of coordinated H_2O molecules within the coordination sphere of the Eu^{3+} ion. Table 2 summarizes the preeminent FT-IR bands of the DO and europium samples. The FT-IR of the europium series exhibits similarities in spectral features, so illustrations of all the FT-IR windows of DO and E5 are displayed in Fig. 3(a and b). Moreover, the spectrum of DO represents bands at 1370 cm^{-1} and 1044 cm^{-1} attributed to CH_3 bending and stretching vibrations of the alkoxy C–O, respectively. The spectrum of the E5 sample portrays bands at 1738 cm^{-1}, 1667 cm^{-1}, 1519 cm^{-1}, 1200 cm^{-1}, 585 cm^{-1} and 482 cm^{-1} ascribed to the stretch vibrations of C=O of ester, C=O of keto, C=N, C–O, Eu–N and Eu–O, respectively. Moreover, the bands within the 1305–1058 cm^{-1} domain are attributed to C–N, C–C and C–O stretching modes, while the band at 1431 cm^{-1} appears owing to the aromatic ring skeletal vibrations.

Table 2 Prominent FT-IR bands (cm^{-1}) of the DO and E1–E5 samples

Complex	ν (C=O)	ν (C–O)	ν (C=N)	ν (Eu–N)	ν (Eu–O)
DO	1717 (s)	1217 (m)	—	—	—
E1	1729 (m)	1198 (m)	—	—	470 (w)
E2	1741 (m)	1203 (m)	1533 (m)	577 (w)	481 (w)
E3	1735 (m)	1194 (m)	1523 (m)	582 (w)	473 (w)
E4	1744 (m)	1197(m)	1527 (m)	580 (w)	479 (w)
E5	1738 (m)	1200 (m)	1519 (m)	585 (w)	482 (w)

3.5 NMR spectral analysis

The NMR spectra of DO as well as of the Eu(III) series were obtained in DMSO utilizing a Bruker Avance II 500 NMR spectrometer. Fig. 4(a) portrays the ^{1}H NMR spectrum of free DO, revealing a triplet in the region of 1.24–1.26 ppm assigned to methyl protons and a quartet in the region of 4.24–4.25 ppm attributed to methylene protons of the ester moiety, which are deshielded due to the adjacent free carbonyl group. A triplet and quartet signal detected in the regions 1.15–1.18 ppm and 4.12–4.13 ppm are attributed to the methylene protons and methyl protons of the second ester moiety, respectively. Furthermore, a doublet appearing at 1.87 ppm corresponds to the signals of methyl protons, and a quartet appearing in the range of 4.02–4.06 ppm corresponds to the C–H proton of carbon having carbonyl functionalities. However, the proton NMR spectra of the europium series exhibit noteworthy variations in the values of the chemical shift because of the magnetic anisotropic

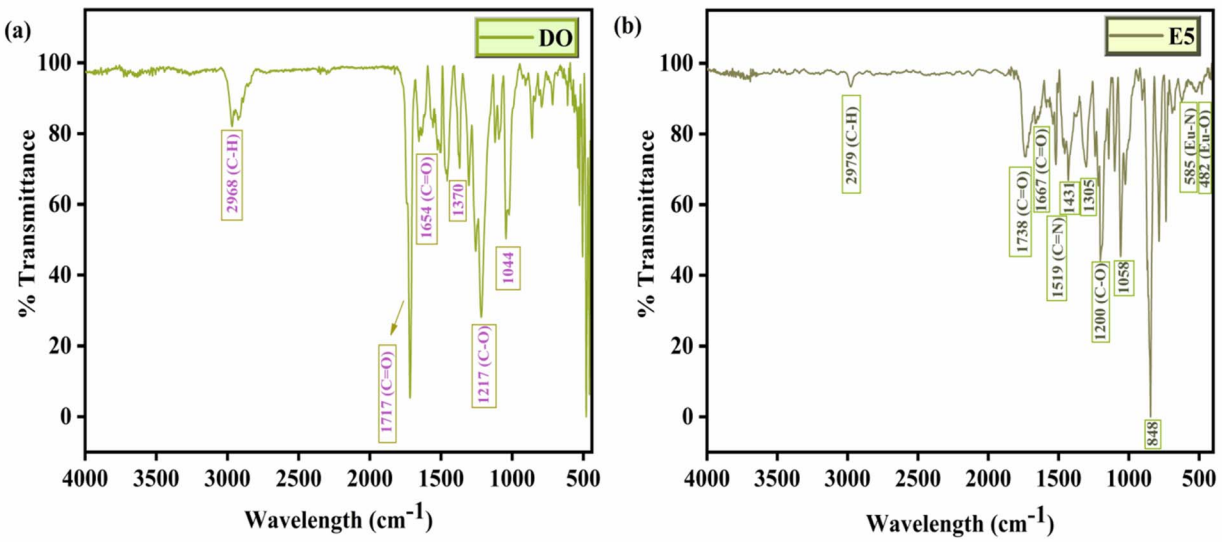

Fig. 3 (a): FT-IR window (in cm^{-1}) of DO. (b): FT-IR window (in cm^{-1}) of E5 [$Eu(DO)_3phen$].

nature of the europium ions. Furthermore, the broadening of certain signals in the spectra of samples is associated with the strong paramagnetic behaviour of the europium center.[39] The complexation of secondary sensitizers in E2–E5 samples is validated by the emergence of additional signals in the region 7.27–9.16 ppm.[15] The proton NMR of the europium series exhibits similarities in spectral features, so illustrations of all the proton NMR windows of E5 are represented in Fig. 4(b).

Further, ^{13}C NMR of the europium series was also analysed to confirm the binding sites in these photoluminescence samples.

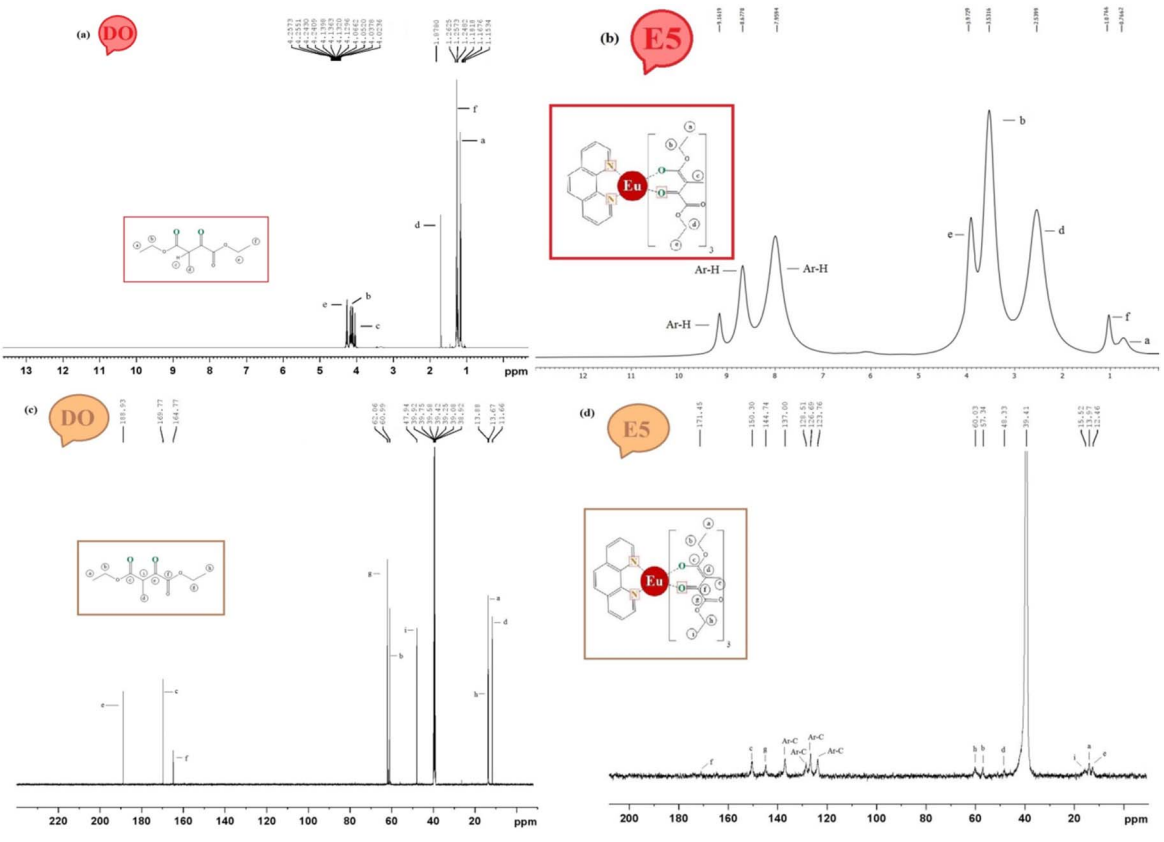

Fig. 4 (a): ^1H NMR signals (in ppm) of DO. (b): ^1H NMR signals (in ppm) of E5 [$Eu(DO)_3phen$]. (c): ^{13}C NMR signals (in ppm) of DO. (d): ^{13}C NMR signals (in ppm) of E5 [$Eu(DO)_3phen$].

Fig. 4(c) displays the spectrum of uncoordinated DO, revealing signals at 164.77 ppm and 169.77 ppm ascribed to the C=O carbon of the ester moiety bonded to the carbonyl group of the ketone and carbonyl carbon of the second ester moiety, respectively, while the signal at 188.93 ppm corresponds to the carbon of the ketone moiety. Further, the signals attributed to $-CH_3$ and $-CH_2$ carbon of ester moiety appear at 13.67 ppm and 60.99 ppm, while the signals attributed to $-CH_3$ and $-CH_2$ carbon of ester moiety adjacent to carbonyl group of ketone appear at 13.88 ppm and 62.06 ppm, respectively. The signal at 47.94 ppm is assigned to the C atom bonded to the carbonyl functionalities, and the signal at 11.66 ppm is attributable to the methyl group associated with this carbon. However, the signals observed at 169.77 ppm and 188.93 ppm in the spectrum of the uncoordinated ligand shift to 150.30 ppm and 171.45 ppm, respectively, in the ^{13}C NMR spectrum of the E5 sample. These variations in the values of the chemical shift provide strong evidence for the complexation of the metal ion with DO *via* the O atom of the ketonic and ester moiety.[40] Additionally, the emergence of new signals in the region 123.76–137.00 ppm validates the coordination of secondary sensitizers with europium ions. Fig. 4(d) depicts the ^{13}C NMR spectral window of the E5 sample.

3.6 Thermal analysis

DTG (differential thermogravimetric analysis) and TGA (thermogravimetric analysis) were analysed to determine the thermal behaviour of the europium series. The thermal analysis of the samples was carried out from ambient temperature to 650 °C by employing a heating rate of 10 °C min^{-1} in an atmosphere of dinitrogen. The primary decomposition phase of the $[Eu(DO)_3$-phen] sample occurs with an inflection in the range of 190.69–419.57 °C accompanied by a weight loss of 61.50% (theoretical loss is 64.50%). This step contributes to the expulsion of the three molecules of the primary sensitizer (DO) from the coordination environment. The second decomposition step exists in the range of 419.57–504.84 °C, resulting in a weight loss of 16.95% (theoretical loss is 19.25%). This inflection is associated with the expulsion of the secondary sensitizer (1,10-phenanthroline). Beyond 504.84 °C, the thermogram portrays a residual mass of 21.55%, which is ascribed to the formation of terbium oxide. Furthermore, this interpretation is supported by the DTG analysis, which exhibits distinct peaks within the same temperature range. The europium series exhibits similarity in thermograms, displaying a similar two-step weight loss pattern, so illustrations of all the decomposing behaviours of E5 are depicted in Fig. 5. The E5 sample exhibits thermal stability of up to 190.69 °C, reflecting greater thermal robustness than the complexes reported by Kumar *et al.*[41] and Khanagwal *et al.*,[42] which exhibit stability of up to 146 °C and 155 °C. The notable thermal stability exhibited by these europium samples highlights their potential applicability in the development of luminescent thin films.[43]

3.7 UV-visible absorption and optical band gap analysis

The UV-visible absorption pattern of DO as well as europium samples was monitored in DMSO (dimethyl sulfoxide). The absorption spectra obtained displayed a band attributed to $\pi \rightarrow \pi^*$ transitions within 280–324 nm and 280–370 nm spans for the DO and E1–E5 complexes, respectively. The maximum of the band is at 288 nm for DO, while for E1–E5 complexes, it has maxima within the 290–296 nm span. The red shift of 2–8 nm recorded in E1–E5 complexes was the consequence of the extended conjugated structure in europium complexes.[44] Fig. 6 portrays the absorbance profiles of the DO and E1–E5 complexes.

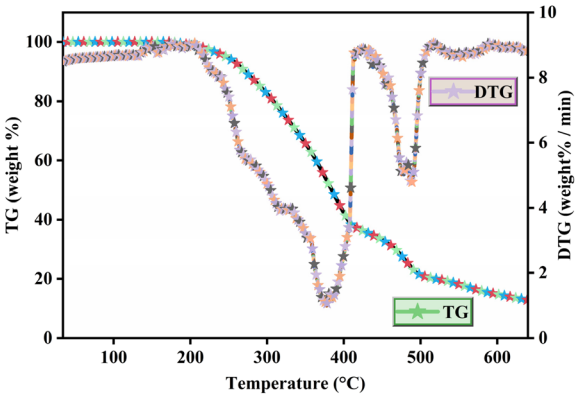

Fig. 5 Thermogram of E5 $[Eu(DO)_3phen]$ in an atmosphere of dinitrogen.

The energy band gap for the DO and E1–E5 complexes was analysed by diffuse reflectance spectra in a wavelength span of 200–800 nm, with barium sulphate utilized as a standard reference. The optical energy band gap (E_g) values were computed by implementing Kubelka–Munk's theory. Kubelka–Munk expression describes the correlation among S (scattering coefficient), R_∞ (recorded reflectance) and K (absorption coefficient) as follows:[45]

$$F(R_\infty) = \frac{(1 - R_\infty)^2}{2R_\infty} = \frac{K}{S}. \quad (3)$$

The values of E_g were determined by implementing Tauc's relation as indicated below:[46]

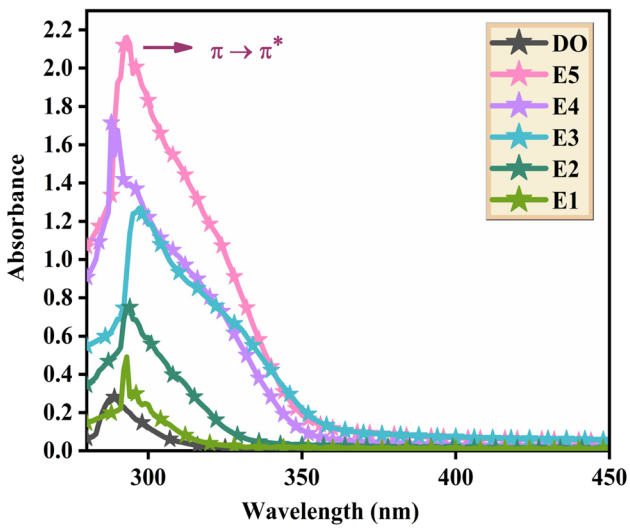

Fig. 6 UV-visible absorbance pattern of the DO and E1–E5 samples.

$$[h\nu F(R_\infty)]^n = C(h\nu - E_g), \quad (4)$$

where C denotes the constant of proportionality, ν represents the frequency of the photon and n value is dependent on the kind of electronic transition with values 2, 1/2, 3/2 and 3 for directly permitted, indirectly permitted, directly prohibited and indirectly prohibited, respectively. Thereafter, the energy gap of the DO and E1–E5 complexes was obtained from the graph of $[F(R_\infty)h\nu]^2$ *vs.* $h\nu$ by the extrapolation of the straight region of the curve up to $[F(R_\infty)h\nu]^2 = 0$.[47] The E_g values obtained for the europium complexes were less than those of DO, indicating a decline in the energy gap of HOMO and LUMO ascribed to the enlarged conjugated structure in Eu^{3+} complexes. Table 3 illustrates the band gap data of DO and europium complexes lying in the same domain as wide band semiconductors (2–4 eV), indicating their applicability in OLEDs, biological sensing and semiconducting devices. Fig. 7(a) and (b) display the Tauc plots of the DO and E5 samples, with the inset displaying their diffuse reflectance spectra.

The values of the band-gap (E_g) were employed to assess the refractive index (n) values for the DO and europium complexes using the following formula:

$$\frac{(n^2-1)}{(n^2+1)} = 1 - \sqrt{\frac{E_g}{20}}. \quad (5)$$

Table 3 illustrates the refractive index values evaluated for the DO and E1–E5 complexes. The results appear to be similar to those of semiconducting metal oxides, demonstrating the potential use of these complexes in photovoltaic devices.[48]

3.8 Computational modelling

Density functional theory (DFT) is an extensively employed computational approach for investigating the optical attributes of synthesized samples. The frontier orbitals, often termed LUMO (lowest unoccupied molecular orbital) and HOMO (highest occupied molecular orbital), were analyzed to gain insights into the chemical reactivity and electronic nature of the europium series. The molecular structures of the complexes were initially generated using the Avogadro program. The geometry of the samples was optimized utilizing its auto optimization tool until it reached a minimum energy state ($dE = 0$).[49] The resulting optimized geometries were employed for further computational evaluations. The frontier molecular energies were computed *via* the B3LYP DFT level. The energies of frontier orbitals, energy difference within HOMO–LUMO and optimized geometries of the DO and europium series are portrayed in Fig. 8. The difference in energy between LUMO and HOMO levels is associated with the chemical activity of molecules. The values of band gap determined theoretically for E1–E5 samples were 3.75, 3.69, 3.61, 3.54 and 3.34 eV, which align well with the values evaluated experimentally *via* Tauc's plot that are 3.79, 3.72, 3.64, 3.55 and 3.36 eV, confirming the reliability of the computational analysis. Since the band gap lies within the wide band semiconductors (2–4 eV) range, these samples serve as promising contenders for usage in OLEDs, military radars and laser technology.

Further, Koopman's theorem, as shown below, was employed to determine the electron affinity and ionization potential of the europium samples:[50]

$$IE = -E_{HOMO},\ EA = -E_{LUMO}. \quad (6)$$

The values of electron affinity and ionization potential enabled the evaluation of various global reactivity descriptors, like ionisation potential (μ), chemical hardness (η), electronegativity (χ) and chemical softness (σ), as given in the following equations:[51]

$$\eta = \frac{IE - EA}{2},\ \chi = \frac{IE + EA}{2},\ \sigma = \frac{1}{\eta},\ \mu = -\chi. \quad (7)$$

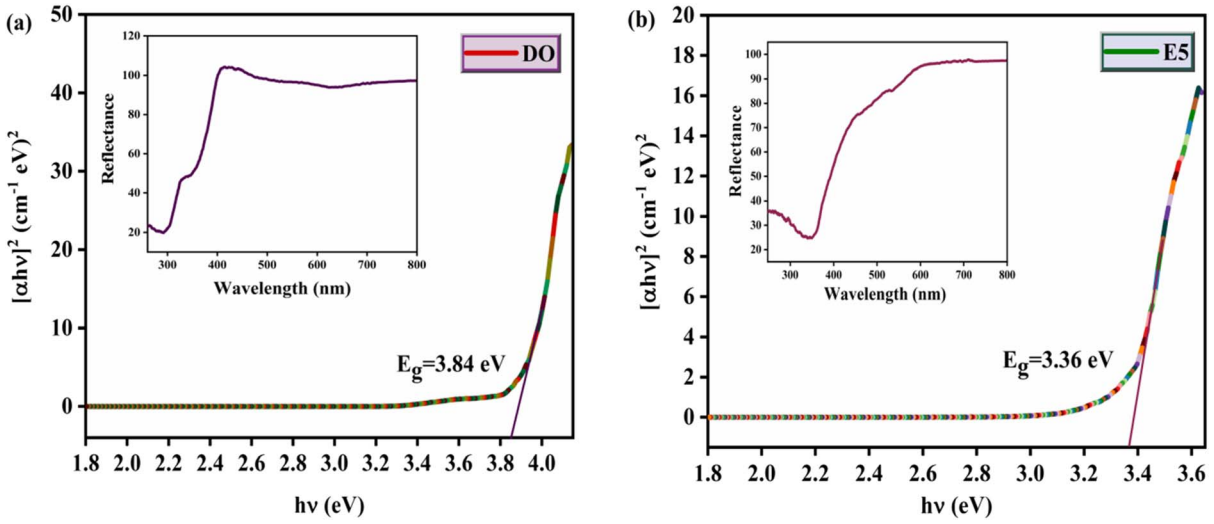

Fig. 7 (a): Tauc plot of DO with the inset displaying its resultant DR spectra. (b): Tauc plot of the E5 [Eu(DO)$_3$phen] sample with the inset displaying its resultant DR spectra.

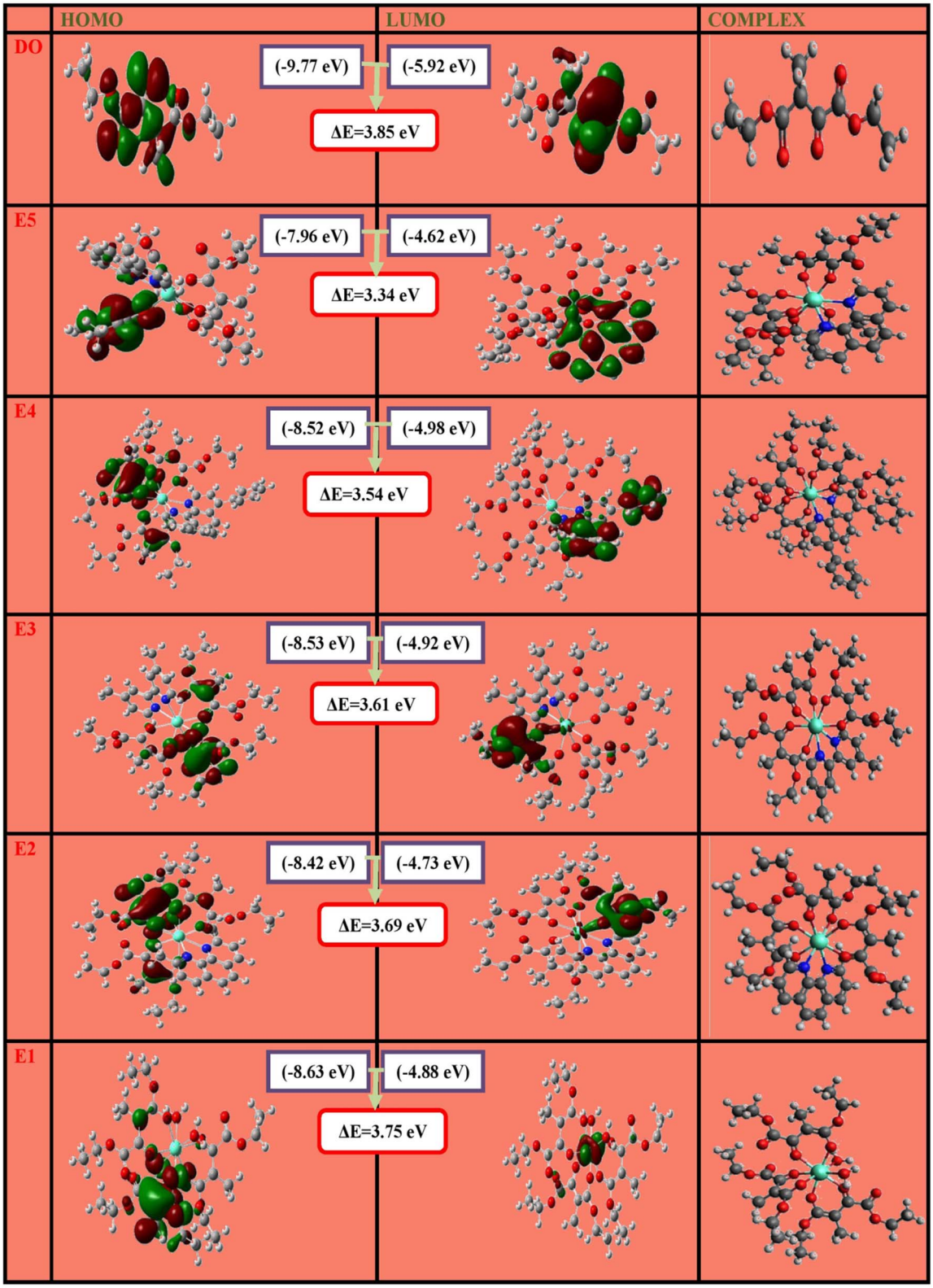

Fig. 8 Band gap and HOMO–LUMO values of the DO and E1–E5 samples.

These descriptors offered valuable insights into the electronic characteristics and reactive tendencies of the europium samples. Table 5 enlists the data of these parameters.

3.9 Photoluminescence studies

The Hitachi F-7000 fluorescence spectrophotometer paired with an Xe (xenon) lamp was utilized to examine the photoluminescence attributes of E1–E5 samples.

The photoluminescence excitation spectral window of europium complexes was recorded between 200 and 450 nm spanned by subjecting them to the dominant emission transition $^5D_0 \rightarrow {}^7F_2$ of the Eu(III) ion. The broadband existing from 300–400 nm with maximum excitation at 360 nm in the spectral profile of europium complexes attributed to the $\pi \rightarrow \pi^*$ transition of the ligand confirms that the bonded ligands have sensitized the Eu(III) ion.[20] The photoluminescence excitation spectra of the E1–E5 complexes are portrayed in Fig. 9.

The emissive profile of the europium complexes in the solid and solution phases (DMSO) was measured in the 450–700 nm range by exciting them at their maximum excitation wavelength. The spectra of E1–E5 complexes in both states portrayed well-resolved emission transitions of the europium ion emanating from the $^5D_0$ excited state to various ^7F_J ground states. The peaks noticed in solid state spectra at 584, 596, 616 and 655 nm and in solution state spectra at 579, 592, 614 and 651 nm are attributed to $^5D_0 \rightarrow {}^7F_J$ ($J = 0, 1, 2, 3$) transitions, respectively. The transition $^5D_0 \rightarrow {}^7F_0$ is electrically and magnetically forbidden, resulting in a weak peak at 584 nm in the solid phase and at 579 nm in the solution phase. The magnetically allowed dipole transition $^5D_0 \rightarrow {}^7F_1$ remains uninfluenced by the chemical field around the europium ions. This transition can be utilized to calibrate the emission spectra of complexes.[27] The emission spectra are dominated by a hypersensitive transition ($^5D_0 \rightarrow {}^7F_2$) that is responsible for the magnificent red emission of europium samples. The intensity of this electric dipole transition $^5D_0 \rightarrow {}^7F_2$ varies strongly with the nature of the ligands and the site symmetry around the europium ions. Hence, the dominating nature of this transition revealed the asymmetry around the europium ions.[52] The transition $^5D_0 \rightarrow {}^7F_3$ is also forbidden in both magnetic and electric dipole schemes, resulting in a faint intensity peak at 655 nm in the solid state and at 651 nm in the solution state. The luminosity of the ternary complexes (E2–E5) was significantly greater than that of the hydrated complex (E1), confirming that the addition of secondary ligands protected the central metal ions from nonradiative deactivation. Fig. 10(a) and (b) depict the photoluminescence emission profile of E1–E5 complexes in the solid and solution phases.

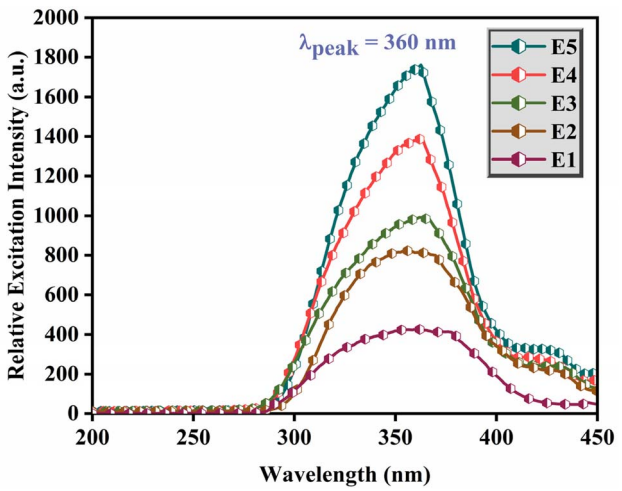

Fig. 9 Photoluminescence excitation spectral window of the E1–E5 samples.

The photoluminescence decay profile of the europium complexes was recorded using the emission wavelength of the dominating transition (616 nm) and the maximum excitation wavelength (360 nm). The decay profile of photoluminescence lifetime was fitted in accordance with the monoexponential expression as stated below:[53]

$$I = I_0 e^{\frac{-t}{\tau}}, \quad (8)$$

where τ is the decay time of photoluminescence and I and I_0 denote the intensity of emission at time t and 0, respectively. The monoexponential behaviour of these decay curves specifies the presence of a single emitting species in the europium samples. The values of photoluminescence decay time for E1–E5 complexes are compiled in Table 3, and the decay curves of europium complexes are portrayed in Fig. 11. The values of the photoluminescence lifetime for the E1–E5 sample lie within 0.71–1.40 ms. These values are higher than the Eu(III) samples previously reported by Wang *et al.*[54] and Bedi *et al.*,[55] whose values lie within 0.115–0.460 ms and 0.186–0.991 ms, respectively. The relatively prolonged lifetime of the E1–E5 samples supports the transmission of energy from the triplet state of the ligand to the resonating levels of the europium ion as the principal route of emission, instead of direct 4f–4f excitation. This phosphorescence mechanism includes the photoexcitation of the sensitizers from the ground singlet (S_0) to the excited singlet (S_1) level after which the excited triplet (T_1) level of sensitizers is populated *via* ISC. Thereafter, the energy is relayed to the resonating levels of Eu(III). Moreover, a significant enhancement in decay time values in E2–E4 complexes is observed because of the replacement of solvent molecules by secondary sensitizers, thus minimizing the radiationless energy loss brought about by OH vibrations.[12]

The integrated intensity ratio (R) of the electrically allowed dipole transition ($^5D_0 \rightarrow {}^7F_2$) to the magnetically allowed dipole transition ($^5D_0 \rightarrow {}^7F_1$) can be employed to determine the extent of the asymmetric field surrounding the europium ion.[56] In the solid phase, the values of the intensity ratio for the E1–E5 samples are 2.45, 2.67, 4.82, 4.79 and 5.44, whereas in the solution phase, these values are 2.53, 3.58, 4.97, 5.81 and 8.14. The values of the intensity ratios are higher in the solution state, indicating a highly asymmetric environment around the europium ions. Furthermore, the branching ratio (β) was computed for each transition by dividing the integrated area of that emission peak by the total integrated area of all the emission

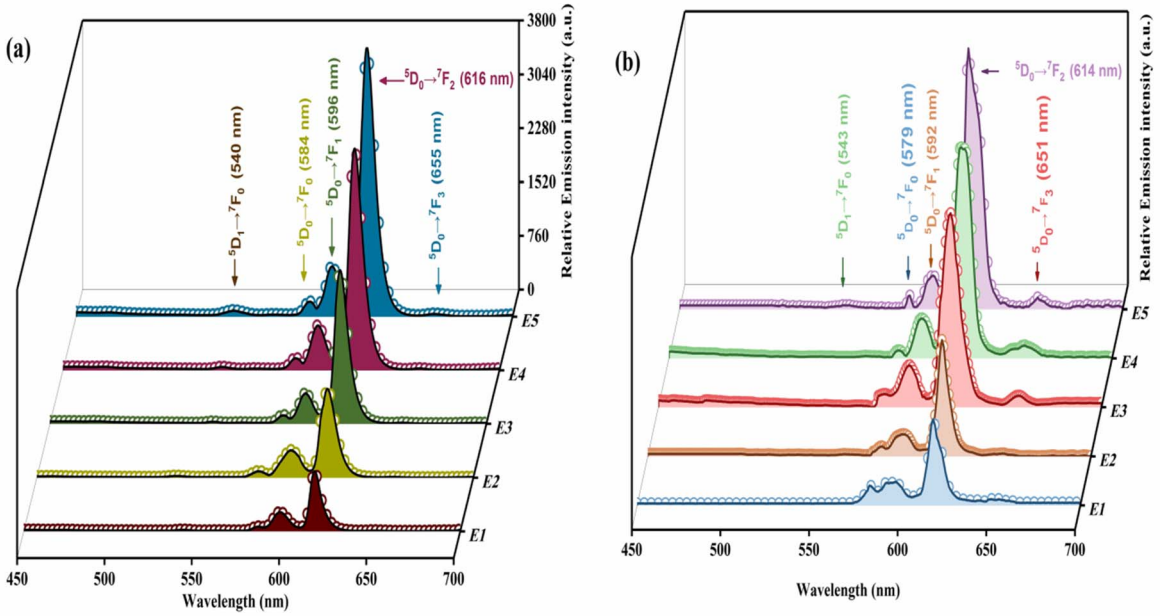

Fig. 10 (a): Photoluminescence emission spectral window of the E1–E5 samples in the solid state. (b): Photoluminescence emission spectral window of the E1–E5 samples in DMSO.

peaks. The values of β computed for the dominant transition ($^5D_0 \rightarrow {}^7F_2$) were in the range of 66.82–80.54% for solid state and in the range of 57.53–77.22% in the solution phase, revealing the utility of these europium samples in the fabrication of laser diodes.[57] The values of R (integrated intensity ratio) and β (branching ratio) are listed in Table 6.

3.10 Judd–Ofelt analysis

In 1962, the Judd–Ofelt theory was developed by G. S. Ofelt and B. R. Judd independently to interpret the intensities of 4f–4f transitions.[58,59] The Judd–Ofelt intensity parameters are computed using the Judd–Ofelt theory by encompassing the data from dynamic coupling and electric dipole transition ($^5D_0 \rightarrow {}^7F_2$). These parameters are sensitive to the asymmetric environment surrounding the europium ion. The Judd–Ofelt intensity parameter (Ω_2) attributed to the $^5D_0 \rightarrow {}^7F_2$ electronic transition was evaluated using the following equation:[60]

$$\Omega_\lambda = 3 \cdot h \cdot A_{0J} \Big/ 64 \cdot \Pi^4 e^2 \bar{\nu}^3 \chi < {}^5D_0 \| U^\lambda \| {}^7F_J >^2, \quad (9)$$

where $\bar{\nu}$ denotes wavenumber of transition, e represents the charge of an electron, h represents Planck's constant, n represents the refractive index ($n \approx 1.5$) and χ represents the Lorentz local field correction [$\chi = n^2(n^2 + 2)^2/9$]. The term $< {}^5D_0 \| U^\lambda \| {}^7F_J >^2$ in eqn (9) is a doubly reduced matrix element, and its value is 0.0032 for $J = 2$ and 0.0023 for $J = 4$.[61]

A_{0J} is the coefficient of emission attributed to $^5D_0 \rightarrow {}^7F_J$ transitions and is evaluated for each transition by utilizing the following equation:

$$A_{0J} = A_{01} \left(\frac{I_{0J}}{I_{01}} \right) \left(\frac{\nu_{01}}{\nu_{0J}} \right), \quad (10)$$

where ν_{0J} and I_{0J} represent barycenter energy and integrated peak areas for $^5D_0 \rightarrow {}^7F_J$ ($J = 0, 1, 2, 3$) transitions, respectively. A_{01} signifies Einstein's coefficient of spontaneous emission corresponding to the $^5D_0 \rightarrow {}^7F_1$ transition and has a value of 50 s^{-1}. A_{01} can serve as a reference to evaluate the values of A_{0J} on account of the fact that its value does not fluctuate with the chemical field around the europium ion.[62]

The intrinsic quantum efficiency (Φ_{Ln}) can be determined by dividing the radiative rate (A_R) by the sum of the nonradiative (A_{NR}) rate and radiative rate assuming that the $^5D_0$ excited state can depopulate only through nonradiative and radiative processes. The expression for determining Φ_{Ln} is given below:[63]

$$\Phi_{Ln} = \frac{A_{rad}}{A_{rad} + A_{nrad}}. \quad (11)$$

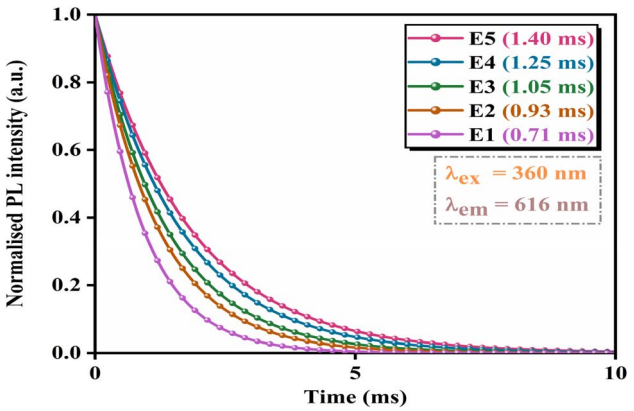

Fig. 11 Photoluminescence decay graph of the E1–E5 samples.

Table 3 Band gap (E_g), refractive indices (n), photoluminescence lifetime (τ) values, intrinsic quantum efficiency (Φ_{Ln}), efficacy of ligand sensitization (η_{sen}) and photoluminescence quantum yield (Φ_t) of the E1–E5 samples

Complex	E_g (eV) (experimental)	Refractive index (n)	τ (ms)	Φ_{Ln} (%)	η_{sen} (%)	Φ_t (%)
E1	3.79	1.90	0.71	13.48	40.13	5.41
E2	3.72	1.91	0.93	18.52	48.43	8.97
E3	3.64	1.92	1.05	33.68	54.51	18.36
E4	3.55	1.94	1.25	40.00	57.95	23.18
E5	3.36	1.97	1.40	49.29	58.63	28.90

The denominator of the aforementioned expression is computed using the decay time of luminescence as given below:[44]

$$\frac{1}{\tau} = A_R + A_{NR} \quad (12)$$

A_R can be evaluated by adding together the A_{0J} associated with each $^5D_0 \rightarrow {}^7F_{J=0,1,2,3}$ transition displayed in the emission spectra of the europium complexes.

$$A_R = \sum_{J=0,1,2,3} A_{0J} = A_{00} + A_{01} + A_{02} + A_{03}. \quad (13)$$

The value of the intrinsic quantum efficiency for E1–E5 complexes is within the 13.48–49.29% range, which is higher than the intrinsic quantum efficiency of complexes reported by Dhankhar *et al.* (6.82–32.56%)[11] and lower than the data reported by Ilmi *et al.* (66–70%).[21] The E2–E5 complexes exhibit a higher value of quantum efficiency compared to the E1 complex owing to the synergistic impact of the secondary ligands and lesser radiationless deactivation. Moreover, the value of Ω_2 for the europium complexes was found to be in the 4.38–9.76 $\times 10^{-20}$ cm^2 range for the solid state and the 4.87–14.85 $\times 10^{-20}$ cm^2 range for the solution state. The higher values of Ω_2 in the solution phase further confirm a more asymmetric surrounding around the metal ions in the solution state. The E1–E5 samples reveal different quantum efficiencies, as each sample exhibits different radiative and non-radiative decay rates owing to the existence of different secondary sensitizers in these samples. These ancillary ligands have different steric effects and electronic structures, such as phen and batho, with the extended delocalisation of electrons in comparison to neo and dmbipy. Thus, the E4–E5 sample reveals high photoluminescence intensity and higher radiative decay, resulting in high quantum efficiency. In sample E2–E3, the C–H oscillators of CH_3 increase the non-radiative decay relative to E4–E5, thus exhibiting low quantum efficiency. The surge in the value of Ω_2 for the E2–E5 complexes compared to the E1 complex shows that the addition of secondary sensitizers in the inner coordination sphere of ternary samples enhanced the asymmetry around the europium ion.[64] Table 4 enlists the data of the radiative decay rate, nonradiative decay rate and Ω_2 parameters of E1–E5 complexes in the solid and solution states. The data of radiative decay rate and Ω_2 for E1–E5 samples in the solid state lie within 190.45–353.79 s^{-1} and 4.38–9.76 $\times 10^{-20}$ cm^2, respectively, which are relatively higher than the data reported by Kumari *et al.*,[65] Hooda *et al.*[66] and Ahlawat *et al.*.[67] The values of radiative decay rate for these reported complexes lie within 136.68–200.3 s^{-1}, 142.73–220.41 s^{-1} and 113.72–165.66 s^{-1}, while the data of Ω_2 lie within 3.91–4.77 $\times 10^{-20}$ cm^2, 2.86–5.44 $\times 10^{-20}$ cm^2 and 0.76–1.30 $\times 10^{-20}$ cm^2, respectively.

The photoluminescence quantum yield of the europium series was determined by utilizing the relation provided below:

$$\Phi_t = \Phi_{Ln} \times \eta_{sen}, \quad (14)$$

where η_{sen} represents the efficacy of ligand sensitization, Φ_{Ln} represents the intrinsic quantum efficiency and Φ_t denotes the quantum yield. These Eu(III) samples exhibit photoluminescence quantum yield within a 5.41–28.90% range, underscoring the efficient transmission of energy from sensitizers to the metal center. The data of Φ_{Ln}, Φ_t and η_{sen} are enlisted in Table 3. The E2–E5 samples exhibit a higher quantum yield than the E1 sample, revealing that the incorporation of secondary sensitizers shields Eu(III) ions from H_2O

Table 4 Radiative decay rate (A_{rad}), nonradiative decay rate (A_{nrad}) and Judd–Ofelt parameter (Ω_2) of the E1–E5 samples

Complex		A_{rad} (s^{-1})	A_{nrad} (s^{-1})	Ω_2 (10^{-20}) cm^2
E1	Solid	190.45	1218.00	4.38
	Solution	232.33	1176.12	4.87
E2	Solid	200.97	874.30	4.78
	Solution	257.37	817.90	6.58
E3	Solid	317.65	634.73	8.62
	Solution	337.92	614.46	8.79
E4	Solid	316.49	483.51	8.59
	Solution	395.99	404.01	10.50
E5	Solid	353.79	360.49	9.76
	Solution	518.57	195.72	14.85

Table 5 Band gap (E_g), chemical hardness (η), chemical softness (σ), electronegativity (χ) and ionisation potential (μ) values of the E1–E5 samples

Complex	E_g (eV) (theoretical)	η	σ	χ	μ
E1	3.75	1.88	0.53	6.76	−6.76
E2	3.69	1.84	0.54	6.58	−6.58
E3	3.61	1.80	0.55	6.72	−6.72
E4	3.54	1.81	0.55	6.75	−6.75
E5	3.34	1.67	0.60	6.29	−6.29

Table 6 Asymmetric ratio (AR) and percentage branching ratio (β) values of the E1–E5 samples

Complex		$^5D_0 \rightarrow {}^7F_0$	$^5D_0 \rightarrow {}^7F_1$	$^5D_0 \rightarrow {}^7F_2$	$^5D_0 \rightarrow {}^7F_3$	$r = I_2/I_1$ (AR)
E1	Solid	4.67	27.32	66.82	0.94	2.45
	Solution	9.29	21.10	57.53	5.76	2.53
E2	Solid	4.09	25.87	69.06	0.58	2.67
	Solution	3.73	17.26	63.52	2.62	3.58
E3	Solid	3.21	16.43	79.14	0.58	4.82
	Solution	2.38	13.77	68.41	3.75	4.97
E4	Solid	3.20	16.50	79.03	0.69	4.79
	Solution	1.30	12.39	73.47	5.62	5.81
E5	Solid	3.14	14.79	80.54	1.05	5.44
	Solution	1.07	9.16	77.22	2.43	8.14

molecules, thereby suppressing the nonradiative deactivation pathways.

3.11 Chromaticity analysis

The CIE 1931 (Commission Internationale de l'Eclairage) chroma coordinates of the europium series were determined by introducing the photoemission data into the MATLAB program. The chroma coordinates obtained for europium complexes in the solid state were 0.603, 0.346 (E1); 0.622, 0.352 (E2); 0.620, 0.339 (E3); 0.623, 0.339 (E4) and 0.628, 0.343 (E5), respectively, and those in the solution state were 0.582, 0.369 (E1); 0.588, 0.352 (E2); 0.597, 0.339 (E3); 0.614, 0.330 (E4); and 0.622, 0.336 (E5), respectively. The values of CIE coordinates turned out to be close to the values of the red illuminant as specified by NTSC (National Television System Committee).[18] Thus, these europium samples can be utilized as a red light emitting component in OLEDs. All the chromaticity coordinates of the solid and solution states lie in the red region of the CIE map, as illustrated in Fig. 12(a) and (b), while the inset portrays the red color emitted by the E5 complex when observed under a UV light source.

Furthermore, the utility of these complexes in advanced optoelectronics can be validated by evaluating the CP (Color Purity) of E1–E5 complexes using the following equation:[68]

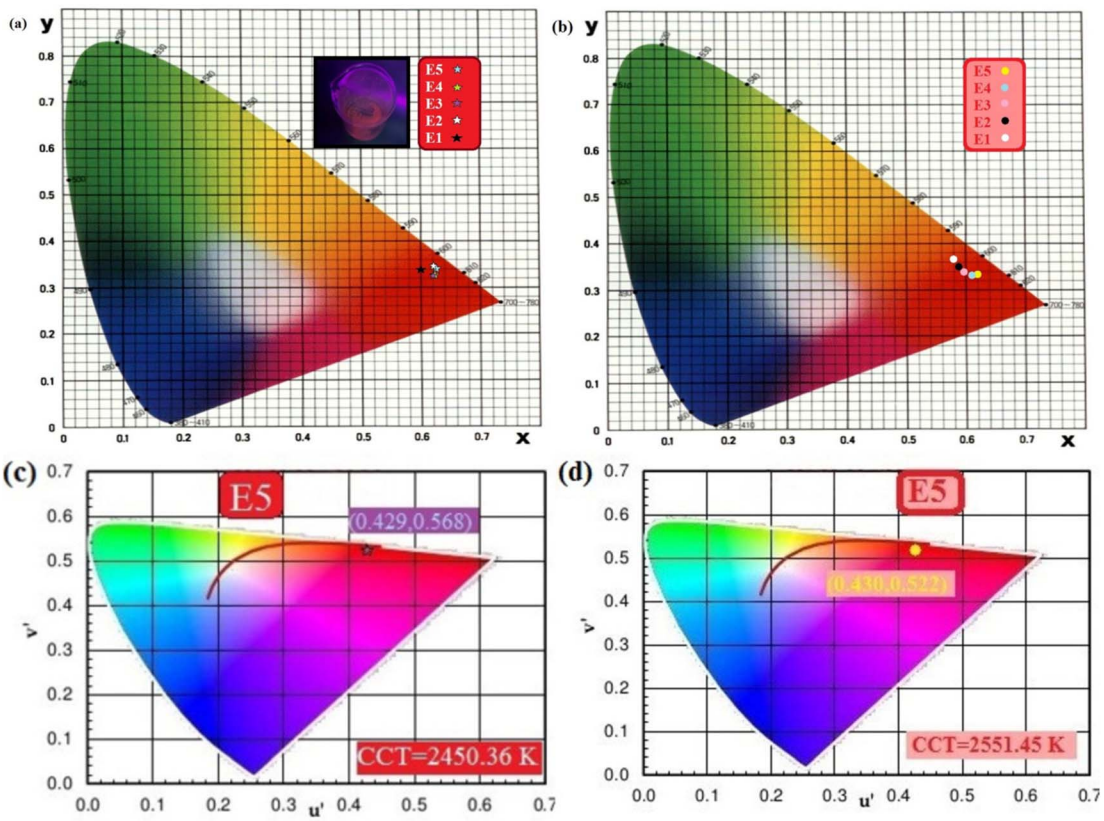

Fig. 12 (a): CIE chromaticity coordinates of the E1–E5 samples in the solid state. (b): CIE chromaticity coordinates of the E1–E5 samples in the solution phase. (c): CIE chart of the E5 sample in the solid state. (d): CIE chart of the E5 sample in the solution phase.

Table 7 CIE chromaticity coordinates (x, y), (u', v') coordinates, CCT and color purity values of the E1–E5 samples

Complex		Color coordinates		Color coordinates		CCT (K)	CP (%)
		x	y	u'	v'		
E1	Solid	0.603	0.346	0.406	0.524	2100.69	82.64
	Solution	0.582	0.369	0.372	0.530	1747.68	76.68
E2	Solid	0.622	0.352	0.416	0.529	2188.23	88.55
	Solution	0.588	0.352	0.389	0.524	1894.94	77.93
E3	Solid	0.620	0.339	0.426	0.524	2444.19	87.76
	Solution	0.597	0.339	0.406	0.519	2162.90	80.74
E4	Solid	0.623	0.339	0.428	0.524	2484.61	88.68
	Solution	0.614	0.330	0.428	0.518	2606.18	83.36
E5	Solid	0.628	0.343	0.429	0.568	2450.36	90.24
	Solution	0.622	0.336	0.430	0.522	2551.45	85.76

$$\mathrm{CP} = \frac{\sqrt{(x - x_i)^2 + (y - y_i)^2}}{\sqrt{(x_d - x_i)^2 + (y_d - y_i)^2}}, \quad (15)$$

where (x_d, y_d), (x_i, y_i) and (x, y) denote the foremost wavelength coordinates, white illumination coordinates and chroma coordinates, respectively. The CP values evaluated for E1–E5 complexes were found to be in the range of 82.64–90.24% in the solid phase and in the range of 76.68–85.76% in the solution phase. The color purity of the samples is higher in the solid phase owing to the narrower emission bands than in the solution state. The previous investigations by Kumar *et al.*[69] and Bedi *et al.*[14] report color purity values of 88.60–98.91% and 64.91–78.11%, respectively, which reveal higher and lower values relative to the present work. The increased color purity of the E2–E5 complexes is attributed to secondary ligands that effectively boost photoluminescence.

The color approach of the emanated light was determined by evaluating the CCT (correlated color temperature) of the complexes. The value of CCT can have a substantial impact on psychological and visible fatigue. The sources of light can be signified as warm, cool and neutral sources of light if their CCTs are below 3200 K, above 4000 K and in the range of 3200–4000 K, respectively. The Mc-Camy formulation given below was utilized to evaluate the CCT of europium complexes:[70]

$$\mathrm{CCT} = -437\,t^3 + 3601\,t^2 - 6861\,t + 5514.31. \quad (16)$$

In the aforementioned relation, $t = (x - x_e)/(y - y_e)$ and the chroma epicenters y_e and x_e have values of 0.186 and 0.332, respectively. The CCT values obtained for europium complexes lie in the range of 2100.69–2484.61 K for the solid phase and in the range of 1747.68–2606.18 K for the solution phase, indicating them as a warm light source and thus revealing the usage of these complexes in dining areas, living rooms and lounges.[71]

Furthermore, another vital color coordinates (u', v') were calculated for europium complexes by utilizing the following equation:[72]

$$v' = \frac{9y}{-2x + 12y + 3}, \quad (17)$$

$$u' = \frac{4x}{-2x + 12y + 3}. \quad (18)$$

The procured data of (u', v') coordinates, color purity, CCT and chroma coordinates are reported in Table 7. The CCT value

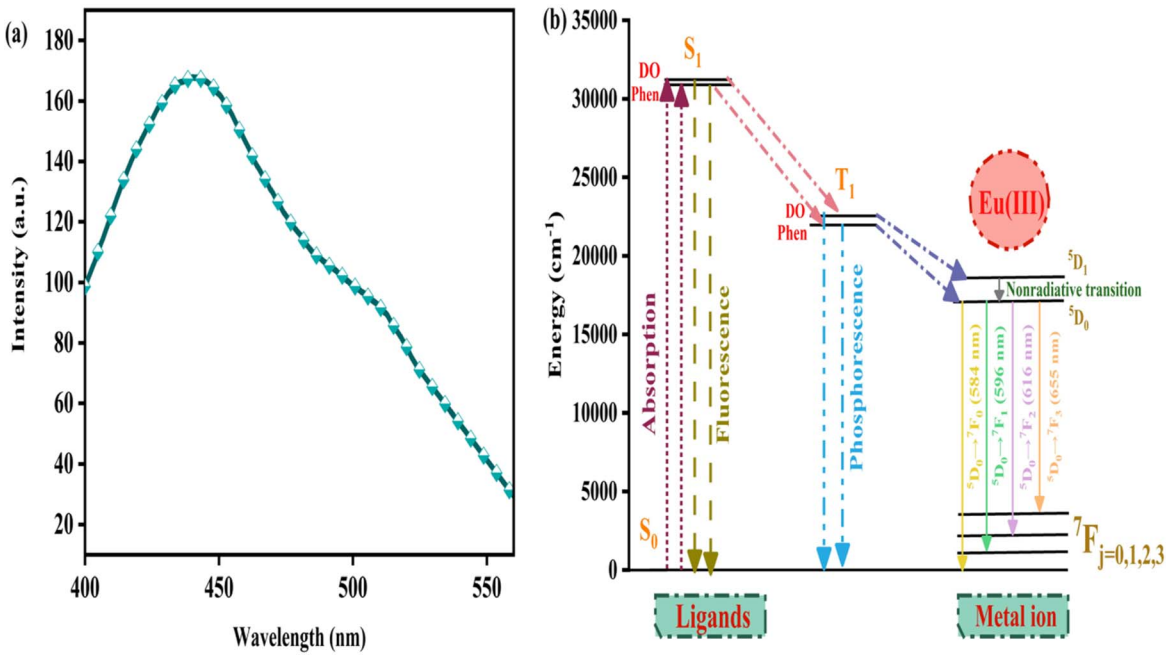

Fig. 13 (a): Phosphorescence spectrum of the G1 [$Gd(DO)_3.2H_2O$] sample. (b) Energy transmission route from sensitizers to Eu^{3+} in the E5 [$Eu(DO)_3$phen] sample.

of E5 in the solid and solution phases is displayed *via* u', v' coordinates in Fig. 12 (c) and (d), respectively.

3.12 Energy transfer mechanism

The intermolecular transmission of energy is the most significant process that determines the photoluminescence parameters of lanthanide complexes. To sensitize the Eu(III) ion, the organic ligands were first excited from the ground singlet (S_0) to the excited singlet (S_1) level, followed by the passing of energy to the excited triplet (T_1) level *via* ISC (intersystem crossing). Thereafter, the energy was transferred to the resonating levels of the europium ion. Finally, in the multiphoton relaxation process, the europium ion emits a red color when the excited state falls to the ground state.[73,74]

In order to achieve adequate energy transmission, the energy difference between the emitting levels of europium ion and T_1 of ligands must be appropriate. As Latva's rule states, this energy difference must be within 2000–5000 cm^{-1}.[75] The efficacy of sensitization is also governed by Reinhoudt's rule. This rule states that for effective ISC, the gap of energy between S_1 and T_1 of organic chromophores must be $\geq$ 5000 cm^{-1}. The energy of the T_1 state of DO was evaluated by the phosphorescence spectrum of the $[Gd(BP)_3(H_2O)_2]$ complex (Fig. 13(a)), while the singlet state was evaluated by its UV-visible absorption spectrum. The dazzling red emission from the europium complexes indicates that the main and secondary sensitizers fulfill the requirements necessary for the adequate transmission of energy, as listed in Table 8. The T_1 and S_1 of secondary ligands are taken from the literature.[66,76] The energy gap between the $^5D_1$ resonating level of Eu^{3+} and the triplet state of DO as well as secondary sensitizers (dmbipy, neo, batho and phen) was found to be 4018, 4226, 3967, 2343 and 3443 cm^{-1}. These values reveal the efficient transmission of energy to the $^5D_1$ level that subsequently relaxes to the $^5D_0$ emissive state through a nonradiative deactivation pathway. The E5 sample possesses the most favourable energy gap compared to the other samples. Hence, based on the combined evaluation of energy difference and luminous intensity, the europium samples were arranged sequentially as E1 < E2 < E3 < E4 < E5. The comparatively weak emission observed in the E1 sample is attributed to the existence of the high frequency O–H vibrations of coordinated H_2O molecules, which facilitate radiationless deactivation of excited emissive levels. Furthermore, in the E2–E5 sample, the sensitizing phenomenon is strengthened by the secondary ligands (neo, dmbipy, batho and phen), resulting in enhanced photoluminescence. The transfer of energy in the E5 complex is depicted in Fig. 13(b).

Table 8 Energy transmission parameters of the DO and secondary sensitizers (neo, phen, batho and dmbipy) in cm^{-1}

Complex	E (S_1)	E (T_1)	ΔE (S_1-T_1)	ΔE_0 (T_1-$^5D_1$)	ΔE_0 (T_1-$^5D_0$)
DO	31 152	22 675	8477	4018	5375
Phen	31 000	22 100	8900	3443	4800
Batho	29 000	21 000	8000	2343	3700
Dmbipy	30 395	22 883	7512	4226	5583
Neo	30 750	22 624	8126	3967	5324

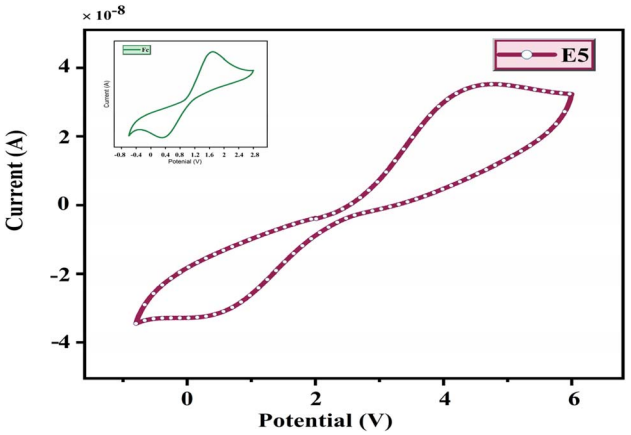

Fig. 14 CV curve of the E5 sample with the inset portraying the CV of ferrocene.

3.13 Cyclic voltammetry analysis

Cyclic voltammetry (CV) assessments were executed to examine the HOMO and LUMO energy levels of the complexes, providing insight into their electrochemical attributes. The electrochemical setup consisted of a platinum wire counter electrode, a glassy carbon working electrode and an Ag/AgCl reference electrode.[77] The CV curve of the E5 sample with the inset portraying the CV of ferrocene is illustrated in Fig. 14. The $E_{1/2}$ of ferrocene was evaluated to be 1.03 V.[29] The redox characteristics of the E_5 sample are crucial for evaluating the energies of frontier molecular orbitals (FMO). The HOMO and LUMO energies are evaluated using the following equations:[78,79]

$$E_{HOMO} = -[E_{ox} - E_{1/2(ferrocene)} + 4.8]\ eV, \quad (19)$$

$$E_{LUMO} = -[E_{red} - E_{1/2(ferrocene)} + 4.8]\ eV. \quad (20)$$

The values of HOMO, LUMO and optical band gap were determined to be −7.97 eV, −4.64 eV and 3.33 eV, respectively, for the E5 sample. The optical bandgap value computed *via* the Tauc plot and DFT analysis was found to be in close agreement with that determined *via* the CV.

4. Conclusion

In brief, the current work reports the synthesis and characterization of five novel octa-coordinated highly luminous red light emanating europium-based samples incorporating β-ketoester (diethyl oxalpropionate) as the primary sensitizer together with secondary ligands (phen, batho, neo and dmbipy). The coordination of secondary sensitizers with the metal center plays a crucial role by effectively suppressing the nonradiative deactivation pathways associated with bonded H_2O molecules. The molecular composition of the europium samples was assessed through EDAX analysis. FESEM was used to assess the surface

morphology, while PXRD studies offered insights into the crystalline nature of the samples. The remarkable thermal stability possessed by the samples was demonstrated by TG/DTG studies, emphasizing their suitability for integration into photonic gadgets. The band gap evaluated *via* DFT calculations exhibits excellent agreement with Tauc's findings. The photoluminescence analysis portrayed peaks at 655, 616, 596 and 584 nm arising from $^5D_0 \rightarrow {}^7F_J$ ($J = 3, 2, 1, 0$) transitions, respectively. The vivid red emission is primarily governed by the most intense emission centered at 616 nm. The emission profile indicates the suitability of these samples for advanced optoelectronic appliances. The photoluminescence decay curve follows a monoexponential pattern, indicating that the europium samples encompass a single emissive species. The intrinsic quantum efficiency of E1–E5 samples in the region 13.48–49.29% demonstrates their suitability for fabricating photoluminescence materials. The values of the branching ratio underscore the potential of europium samples in laser diodes, while their band gap and refractive indices collectively highlight their utility in semiconducting devices. Photometric analyses, like CIE, CCT and CP, reveal that they function as warm red sources of light, indicating their potential as promising candidates for indoor lighting. The existence of chroma coordinates in the red region of the CIE map indicates the effective transmission of energy and further suggests the applicability of these samples as red emitters in OLEDs.

Author contributions

Nishita Dua: conceptualization, investigation, writing-original draft, visualization, software, data curation, validation, methodology, formal analysis, writing-review & editing. Priti Boora Doon: supervision, resources, writing-review & editing, project administration.

Conflicts of interest

The authors declare no conflict of interest regarding the present research paper.

Data availability

All the information and data related to the research article entitled "Exploring vivid red light emanating europium complexes incorporating β-ketoester antenna for advanced displays: a detailed photophysical, Judd–Ofelt and computational investigation" have already been provided inside the article.

Acknowledgements

Ms. Nishita Dua admiringly acknowledges the University Grants Commission (UGC), New Delhi, India for financial support in the form of a senior research fellowship (SRF, Award No. 201610160643) to accomplish this research work.

References

1 K. N. Shinde and S. J. Dhoble, *Crit. Rev. Solid State Mater. Sci.*, 2014, **39**, 459–479.
2 S. I. Weissman, *J. Chem. Phys.*, 1942, **10**, 214–217.
3 R. Ilmi, J. Yin, J. D. L. Dutra, N. K. Al Rasbi, W. F. Oliveira, L. Zhou, W.-Y. Wong, P. R. Raithby and M. S. Khan, *Dalton Trans.*, 2022, **51**, 14228–14242.
4 W. P. Lustig, S. Mukherjee, N. D. Rudd, A. V Desai, J. Li and S. K. Ghosh, *Chem. Soc. Rev.*, 2017, **46**, 3242–3285.
5 C. D. S. Brites, A. Millán and L. D. Carlos, in *Handbook on the Physics and Chemistry of Rare Earths*, Elsevier, 2016, vol. 49, pp. 339–427.
6 J. Tang and P. Zhang, *Lanthanide Single Molecule Magnets*, Springer, 2015, vol. 2.
7 D. V Lapaev, V. G. Nikiforov, V. S. Lobkov, A. A. Knyazev and Y. G. Galyametdinov, *J. Mater. Chem. C*, 2018, **6**, 9475–9481.
8 P.-P. Sun, J.-P. Duan, J.-J. Lih and C.-H. Cheng, *Adv. Funct. Mater.*, 2003, **13**, 683–691.
9 P. Kumari, V. Lather, S. Khatri, P. Ahlawat, H. Sehrawat, S. P. Khatkar, V. B. Taxak and R. Kumar, *RSC Adv.*, 2022, **12**, 35827–35848.
10 W. Xu, Y. Wang, X. Bai, B. Dong, Q. Liu, J. Chen and H. Song, *J. Phys. Chem. C*, 2010, **114**, 14018–14024.
11 P. Dhankhar, R. Devi, S. Devi, S. Chahar, M. Dalal, V. B. Taxak, S. P. Khatkar and P. Boora, *Rare Met.*, 2022, **41**, 1342–1352.
12 M. L. P. Reddy, V. Divya and R. Pavithran, *Dalton Trans.*, 2013, **42**, 15249–15262.
13 J. P. Leonard and T. Gunnlaugsson, *J. Fluoresc.*, 2005, **15**, 585–595.
14 M. Bedi, M. Punia, V. B. Taxak, S. P. Khatkar and P. B. Doon, *Luminescence*, 2022, **37**, 1098–1108.
15 A. B. Ganaie and K. Iftikhar, *ACS Omega*, 2021, **6**, 21207–21226.
16 L. D. Carlos, C. de Mello Donega, R. Q. Albuquerque, S. Alves Jr, J. F. S. Menezes and O. L. Malta, *Mol. Phys.*, 2003, **101**, 1037–1045.
17 D. A. Komissar, M. T. Metlin, S. A. Ambrozevich, I. V Taydakov, A. S. Tobokhova, E. A. Varaksina and A. S. Selyukov, *Spectrochim. Acta, Part A*, 2019, **222**, 117229.
18 R. Boddula, J. Tagare, K. Singh and S. Vaidyanathan, *Mater. Chem. Front.*, 2021, **5**, 3159–3175.
19 R. Devi, M. Dalal, M. Bala, S. P. Khatkar, V. B. Taxak and P. Boora, *J. Mater. Sci.: Mater. Electron.*, 2016, **27**, 12506–12516.
20 M. Punia and P. B. Doon, *Opt. Mater.*, 2023, **138**, 113714.
21 R. Ilmi, A. Haque and M. S. Khan, *J. Photochem. Photobiol., A*, 2019, **370**, 135–144.
22 R. Ilmi, S. Kansız, N. Dege and M. S. Khan, *J. Photochem. Photobiol., A*, 2019, **377**, 268–281.
23 M. Bala, S. Kumar, R. Devi, V. B. Taxak, P. Boora, S. P. Khatkar and J. Fluor, *Chem*, 2016, **188**, 177–184.
24 D. A. Metlina, M. T. Metlin, S. A. Ambrozevich, I. V Taydakov, K. A. Lyssenko, A. G. Vitukhnovsky, A. S. Selyukov, V. S. Krivobok, D. F. Aminev and A. S. Tobokhova, *J. Lumin.*, 2018, **203**, 546–553.

25 W.-J. Chai, W.-X. Li, X.-J. Sun, T. Ren and X.-Y. Shi, *J. Lumin.*, 2011, **131**, 225–230.
26 P. Nandal, R. Kumar, A. Khatkar, S. P. Khatkar and V. B. Taxak, *J. Mater. Sci.: Mater. Electron.*, 2016, **27**, 878–885.
27 R. Ilmi, A. Haque and M. S. Khan, *J. Photochem. Photobiol., A*, 2019, **370**, 135–144.
28 D. B. A. Raj, B. Francis, M. L. P. Reddy, R. R. Butorac, V. M. Lynch and A. H. Cowley, *Inorg. Chem.*, 2010, **49**, 9055–9063.
29 P. Dixit, S. Bhayana, A. Singh, V. Ghangas, A. Sihmar and S. Khatri, *J. Mol. Struct.*, 2025, **1343**, 142851.
30 S. A. Bhat and K. Iftikhar, *Dyes Pigm.*, 2020, **179**, 108383.
31 R. Ilmi, M. S. Khan, Z. Li, L. Zhou, W.-Y. Wong, F. Marken and P. R. Raithby, *Inorg. Chem.*, 2019, **58**, 8316–8331.
32 F. T. L. Muniz, M. A. R. Miranda, C. Morilla dos Santos and J. M. Sasaki, *Found. Crystallogr.*, 2016, **72**, 385–390.
33 P. Chhillar and P. B. Doon, *Mater. Sci. Eng., B*, 2025, **311**, 117849.
34 R. Gaur, A. Dahiya and P. B. Doon, *Emergent Mater.*, 2025, 1–18.
35 S. Myhajlenko, J. L. Batstone, H. J. Hutchinson and J. W. Steeds, *J. Phys. C:Solid State Phys.*, 1984, **17**, 6477.
36 R. Gaur and P. B. Doon, *J. Mol. Struct.*, 2025, **1335**, 141917.
37 P. Ahlawat, P. Kumari, V. Lather, M. Kumar and R. Kumar, *Spectrochim. Acta, Part A*, 2025, **324**, 124976.
38 M. Bedi, M. Punia, R. Devi, V. B. Taxak, S. P. Khatkar and P. B. Doon, *J. Photochem. Photobiol., A*, 2022, **431**, 114003.
39 S. Khatri, P. Hooda, P. Ahlawat, S. P. Khatkar, V. B. Taxak and R. Kumar, *Res. Chem. Intermed.*, 2022, **48**, 1685–1716.
40 P. Ahlawat, S. Bhayana, V. Lather, S. Khatri, P. Kumari, M. Kumar, M. S. Shekhawat, V. B. Taxak, S. P. Khatkar and R. Kumar, *Opt. Mater.*, 2022, **133**, 112940.
41 S. Kumar, S. Chahar, V. B. Taxak, P. Boora and S. P. Khatkar, *Optik*, 2020, **202**, 163636.
42 J. Khanagwal, R. Kumar, P. Hooda, S. P. Khatkar and V. B. Taxak, *Inorg. Chim. Acta*, 2021, **525**, 120463.
43 S. A. Bhat and K. Iftikhar, *Opt. Mater.*, 2020, **99**, 109600.
44 Y. Luo, B. Chen, W. Wu, X. Yu, Q. Yan and Q. Zhang, *J. Lumin.*, 2009, **129**, 1309–1313.
45 S. Kasturi and V. Sivakumar, *RSC Adv.*, 2016, **6**, 98652–98662.
46 A. Dolgonos, T. O. Mason and K. R. Poeppelmeier, *J. Solid State Chem.*, 2016, **240**, 43–48.
47 P. Chhillar, A. Hooda, V. B. Taxak, S. P. Khatkar and P. B. Doon, *Mater. Chem. Phys.*, 2022, **277**, 125542.
48 N. Dua and P. B. Doon, *J. Mater. Sci.: Mater. Electron.*, 2025, **36**, 534.
49 M. D. Hanwell, D. E. Curtis, D. C. Lonie, T. Vandermeersch, E. Zurek and G. R. Hutchison, *J. Cheminf.*, 2012, **4**, 1–17.
50 T. Koopmans, *Physica*, 1934, **1**, 104–113.
51 R. Vijayaraj, V. Subramanian and P. K. Chattaraj, *J. Chem. Theory Comput.*, 2009, **5**, 2744–2753.
52 M. S. Khan, R. Ilmi, W. Sun, J. D. L. Dutra, W. F. Oliveira, L. Zhou, W.-Y. Wong and P. R. Raithby, *J. Mater. Chem. C*, 2020, **8**, 5600–5612.
53 M. Kumar, P. Ahlawat, P. Kumari, V. Lather and R. Kumar, *Inorg. Chem. Commun.*, 2024, **161**, 112087.
54 D. Wang, C. Zheng, L. Fan, J. Zheng and X. Wei, *Synth. Met.*, 2012, **162**, 2063–2068.
55 M. Bedi, P. Chhillar, P. Dhankhar, J. Khanagwal, V. B. Taxak, S. P. Khatkar and P. B. Doon, *J. Fluoresc.*, 2022, **32**, 1073–1087.
56 K. Binnemans, *Coord. Chem. Rev.*, 2015, **295**, 1–45.
57 N. Dua, M. Punia, P. Chhillar, M. Bedi, S. P. Khatkar, V. B. Taxak and P. B. Doon, *Luminescence*, 2023, **38**, 783–795.
58 G. S. Ofelt, *J. Chem. Phys.*, 1962, **37**, 511–520.
59 B. R. Judd, *Phys. Rev.*, 1962, **127**, 750.
60 R. Ilmi, S. Kansız, N. Dege and M. S. Khan, *J. Photochem. Photobiol., A*, 2019, **377**, 268–281.
61 R. Ilmi, A. Haque, I. J. Al-Busaidi, N. K. Al Rasbi and M. S. Khan, *Dyes Pigm.*, 2019, **162**, 59–66.
62 G. F. De Sa, O. L. Malta, C. de Mello Donegá, A. M. Simas, R. L. Longo, P. A. Santa-Cruz and E. F. da Silva Jr, *Coord. Chem. Rev.*, 2000, **196**, 165–195.
63 V. D. Savchenko, K. P. Zhuravlev and V. I. Tsaryuk, *J. Lumin.*, 2024, **276**, 120839.
64 P. Dhankhar, M. Bedi, J. Khanagwal, V. B. Taxak, S. P. Khatkar and P. B. Doon, *Spectrosc. Lett.*, 2020, **53**, 256–269.
65 P. Kumari, S. Khatri, P. Ahlawat, P. Hooda, V. B. Taxak, S. P. Khatkar and R. Kumar, *J. Chem. Sci.*, 2022, **135**, 2.
66 P. Hooda, V. Lather, R. K. Malik, V. B. Taxak, S. P. Khatkar, S. Khatri, P. Ahlawat and R. Kumar, *Optik*, 2022, **264**, 169389.
67 P. Ahlawat, V. Lather, S. Bhayana, S. Khatri, P. Hooda, P. Kumari, V. B. Taxak, S. P. Khatkar and R. Kumar, *Inorg. Chem. Commun.*, 2022, **142**, 109720.
68 K. Singh, M. Rajendran, R. Devi and S. Vaidyanathan, *Dalton Trans.*, 2021, **50**, 4986–5000.
69 M. Kumar, P. Kumari, V. Lather, P. Ahlawat, A. Khatkar and R. Kumar, *J. Mol. Struct.*, 2023, **1293**, 136213.
70 C. S. McCamy, *Color Res. Appl.*, 1992, **17**, 142–144.
71 P. Khajuria, R. Mahajan, S. Kumar, R. Prakash, R. J. Choudhary and D. M. Phase, *Optik*, 2020, **216**, 164909.
72 J. Andres and A.-S. Chauvin, *Molecules*, 2020, **25**, 4022.
73 Z. Abbas, S. Dasari, M. J. Beltrán-Leiva, P. Cantero-López, D. Páez-Hernández, R. Arratia-Pérez, R. J. Butcher and A. K. Patra, *New J. Chem.*, 2019, **43**, 15139–15152.
74 S. Lis, *J. Alloys Compd.*, 2002, **341**, 45–50.
75 M. Latva, H. Takalob, V. M. Mukkala, C. Matachescu, J. C. Rodríguez-Ubis and J. Kankare, *J. Lumin.*, 1997, **75**, 149–169.
76 M. Punia, P. Dhankhar, N. Dua, V. B. Taxak, S. P. Khatkar and P. B. Doon, *Inorg. Chim. Acta*, 2023, **544**, 121225.
77 V. Aggarwal, D. Singh, A. Hooda, K. Nehra, K. Jakhar, S. Kumar, R. S. Malik and P. Kumar, *J. Mater. Sci.: Mater. Electron.*, 2024, **35**, 1–14.
78 A. Hooda, D. Singh, A. Dalal, K. Nehra, S. Kumar, R. S. Malik, R. Kumar and P. Kumar, *RSC Adv.*, 2023, **13**, 9033–9045.
79 K. Nehra, A. Dalal, A. Hooda, D. Singh, R. S. Malik and S. Kumar, *J. Mater. Sci.: Mater. Electron.*, 2022, **33**, 115–125.